



HAL
open science

MEK-SHP2 inhibition prevents tibial pseudarthrosis caused by NF1 loss in Schwann cells and skeletal stem/progenitor cells

Simon Perrin, Sanela Protic, Vincent Bretegnier, Ingrid Laurendeau, Oriane Duchamp de Lageneste, Nicolas Panara, Odile Ruckebusch, Marine Luka, Cécile Masson, Théodora Maillard, et al.

► To cite this version:

Simon Perrin, Sanela Protic, Vincent Bretegnier, Ingrid Laurendeau, Oriane Duchamp de Lageneste, et al.. MEK-SHP2 inhibition prevents tibial pseudarthrosis caused by NF1 loss in Schwann cells and skeletal stem/progenitor cells. *Science Translational Medicine*, 2024, 16 (753), pp.eadj1597. 10.1126/scitranslmed.adj1597 . hal-04646302

HAL Id: hal-04646302

<https://hal.u-pec.fr/hal-04646302v1>

Submitted on 12 Jul 2024

HAL is a multi-disciplinary open access archive for the deposit and dissemination of scientific research documents, whether they are published or not. The documents may come from teaching and research institutions in France or abroad, or from public or private research centers.

L'archive ouverte pluridisciplinaire **HAL**, est destinée au dépôt et à la diffusion de documents scientifiques de niveau recherche, publiés ou non, émanant des établissements d'enseignement et de recherche français ou étrangers, des laboratoires publics ou privés.

MEK-SHP2 inhibition prevents tibial pseudarthrosis caused by *NF1* loss in Schwann cells and skeletal stem/progenitor cells

Simon Perrin¹, Sanela Protic¹, Vincent Bretegnier¹, Ingrid Laurendeau², Oriane Duchamp de Lageneste¹, Nicolas Panara², Odile Ruckebusch³, Marine Luka^{4,5}, Cécile Masson^{6,7}, Théodora Maillard⁸, Fanny Coulpier¹, Stéphanie Pannier⁹, Philippe Wicart⁹, Smail Hadj-Rabia¹⁰, Katarzyna J. Radomska¹, Mohammed Zarhrate^{7,11}, Mickael Ménager^{4,5}, Dominique Vidaud^{2,8}, Piotr Topilko¹, Béatrice Parfait^{2,8}, and Céline Colnot^{1,*}

¹ Univ Paris Est Creteil, INSERM, IMRB, 94000, Creteil, France

² INSERM UMR S1016, Institut Cochin, Université Paris Cité, 75014, Paris, France

³ Univ Paris Est Creteil, INSERM, IMRB, Plateforme de Cytométrie en flux, 94000, Creteil, France

⁴ Paris Cité University, Imagine Institute, Laboratory of Inflammatory Responses and Transcriptomic Networks in Diseases, Atip-Avenir Team, INSERM UMR 1163, 75015, Paris, France.

⁵ Labtech Single-Cell@Imagine, Imagine Institute, INSERM UMR 1163, 75015, Paris, France.

⁶ Bioinformatics Core Facility, Institut Imagine-Structure Fédérative de Recherche Necker, INSERM U1163, 75015, Paris, France.

⁷ INSERM US24/CNRS UAR3633, Paris Cité University, 75015, Paris, France

⁸ Service de Médecine Génomique des Maladies de Système et d'Organe, Hôpital Cochin, DMU BioPhyGen, Assistance Publique-Hôpitaux de Paris, AP-HP, Centre-Université Paris Cité, F-75014 Paris, France

⁹ Department of Pediatric Orthopedic Surgery and Traumatology, Necker-Enfants Malades Hospital, AP-HP, Paris Cité University, 75015, Paris, France

¹⁰ Department of Dermatology, Reference Center for Rare Skin Diseases (MAGEC), Imagine Institute, Necker-Enfants Malades Hospital, AP-HP, Paris Cité University, 75015, Paris, France.

¹¹ Genomics Core Facility, Institut Imagine-Structure Fédérative de Recherche Necker, INSERM U1163, 75015, Paris, France.

*Corresponding author: celine.colnot@inserm.fr

29 **One Sentence Summary**

30

31 Combined MEK-SHP2 inhibition prevents fibrotic failure to heal in a preclinical model of congenital
32 pseudarthrosis of the tibia.

33 **Abstract**

34 Congenital pseudarthrosis of the tibia (CPT) is a severe pathology marked by spontaneous bone
35 fractures that fail to heal leading to fibrous nonunion. Half of patients with CPT are affected by the
36 multisystemic genetic disorder neurofibromatosis type 1 (NF1), caused by mutations in the *NF1* tumor
37 suppressor gene, a negative regulator of RAS-MAPK signaling pathway. Here, we analyzed patients
38 with CPT and *Prss56-Nf1* knockout mice to elucidate the pathogenic mechanisms of CPT-related fibrous
39 nonunion and explored a pharmacological approach to treat CPT. We identified *NF1*-deficient Schwann
40 cells and skeletal stem/progenitor cells (SSPCs) in pathological periosteum as affected cell types driving
41 fibrosis. Whereas *NF1*-deficient SSPCs adopted a fibrotic fate, *NF1*-deficient Schwann cells produced
42 critical paracrine factors including TGF β and induced fibrotic differentiation of wild-type SSPCs. To
43 target both *NF1*-deficient Schwann cells and SSPCs, we used combined MEK and SHP2 inhibitors to
44 counteract the elevated RAS-MAPK signaling in human SSPCs. Combined MEK-SHP2 inhibition in vivo
45 prevented fibrous nonunion in the *Prss56-Nf1* knockout mouse model, providing a promising therapeutic
46 strategy for the treatment of fibrous nonunion in CPT.

47

48 Introduction

49

50 Congenital pseudarthrosis of the tibia (CPT) is a rare but severe pathology that manifests mostly in
51 children prior to 2 years of age. Patients with CPT present with tibial bowing at birth leading to
52 spontaneous fracture and failure to heal due to fibrous nonunion. CPT treatment is exclusively surgical
53 and remains highly challenging, with substantial risk of re-fracture or amputation (1, 2). Pharmacological
54 treatments are needed to improve CPT management, but the pathogenic mechanisms remain poorly
55 understood and a relevant pre-clinical model for CPT is lacking. CPT can be classified as isolated CPT
56 of unknown etiology, or NF1-related CPT in patients diagnosed with neurofibromatosis type 1 (NF1).
57 NF1 is one of the most common multisystemic genetic disorders that affects 1 in 3000 individuals.
58 Patients with NF1 can exhibit a variety of symptoms, including benign nerve sheath tumors, called
59 cutaneous and plexiform neurofibromas (NFBs), skin hyperpigmentation (Café-au-lait macules,
60 CALMs), learning disabilities, and bone manifestations (3). NF1 is caused by heterozygous mutations
61 in the *NF1* gene encoding the tumor-suppressor neurofibromin, a negative regulator of RAS and the
62 MAPK pathway. The diverse NF1 symptoms result from a second somatic mutational event in specific
63 tissues and cell types. NFBs and CALMs have been shown to result from *NF1* biallelic inactivation in
64 Schwann cells and melanocytes respectively (4–8).

65

66 Although *NF1* biallelic inactivation has been reported in CPT, the specific cell types harboring *NF1* loss
67 have not been identified. The presence of pathological periosteum suggests the involvement of the
68 periosteum in the pathogenesis of CPT (9–11). Located on the outer layer of bones, the periosteum is
69 essential for bone regeneration and contains a major source of skeletal stem/progenitor cells (SSPCs)
70 as well as immune, endothelial, and neural cells (12–18). Until now, investigations of NF1 bone
71 manifestations in mouse models have focused mainly on the skeletal lineage and the consequences of
72 *Nf1* gene inactivation on fracture repair have been examined using bone-specific Cre lines (19–23).
73 However, targeting *Nf1* solely in bone lineages does not recapitulate other NF1 features. Recent work
74 by Radomska et al. reported the *Prss56-Nf1* knockout (KO) mouse model that faithfully recapitulates
75 several NF1 symptoms, demonstrating that *Prss56*-expressing boundary cap (BC) cells are the cellular
76 origin of cutaneous and plexiform NFBs, as well as skin hyperpigmentation (24). Located at the surface
77 of the neural tube during development, BC cells are transient neural crest-derived populations giving
78 rise to various derivatives in nerves and skin such as Schwann cells, fibroblasts, and melanocytes (25).

79 The common BC origin of NF1 dermatological and neurological lesions raises the question of a common
80 cellular origin with NF1 bone manifestations.

81

82 Pharmacological interventions for NF1-related conditions are mostly targeting the RAS-MAPK signaling
83 pathway. Several preclinical studies demonstrated the efficacy of MEK-inhibitors to counteract the
84 elevated RAS-MAPK signaling due to reduced neurofibromin activity in cells lacking *NF1* (26, 27). This
85 led to a successful clinical trial and Food and Drug Administration (FDA) approval of selumetinib in 2020
86 for patients with inoperable plexiform NFBs (27–29). MEK inhibitors have also been tested in animal
87 models exhibiting bone phenotypes associated with *Nf1* loss of function in bone cells but showed limited
88 effects (19, 22). Other approaches such as BMP2, bisphosphonates, lovastatin, and beta-catenin
89 inhibition have also shown variable results (19, 30–32).

90

91 This study aimed to identify the cellular origin and pathogenic mechanisms of CPT to develop efficient
92 therapeutic strategies. Combined analyses of samples from patients with CPT and from the *Prss56-Nf1*
93 KO mouse model unraveled the conserved mechanisms of CPT between mice and humans. We
94 performed genetic analyses of patient pseudarthrosis tissues to search for *NF1* second hit mutations in
95 various cell types in the periosteum including SSPCs and Schwann cells. To elucidate the role of RAS-
96 MAPK pathway overactivation in CPT, we investigated the tibial pseudarthrosis phenotype of *Prss56-
97 Nf1* KO mice that carry *Nf1* gene inactivation in BC derived SSPCs and Schwann cells in periosteum.
98 Based on these results, we posited that combining MEK with SHP2 inhibition would drive robust
99 responses in NF1 bone lesions, as SHP2 is a master positive regulator of RAS-MAPK pathway upstream
100 of RAS (33, 34). We tested the efficacy of combined MEK and SHP2 inhibition to prevent pseudarthrosis
101 in the pre-clinical *Prss56-Nf1* KO mouse model.

102

103

104

105 **Results**

106 **SSPCs and Schwann cells within pathological periosteum carry *NF1* biallelic inactivation in CPT**

107 To investigate the tissue specificity of *NF1* biallelic inactivation in CPT, we performed *NF1* targeted
108 sequencing of tissues from the affected pseudarthrosis (PA) site, the unaffected iliac crest (IC), and
109 blood of 17 patients undergoing surgical treatment (Figure 1A-B, Table S1). We detected *NF1* biallelic
110 inactivation primarily in the periosteum of the PA site (13/17 patients, Figure 1C). We also identified *NF1*
111 biallelic inactivation in fibrous tissue (6/17 patients), bone (6/17) and bone marrow (4/17) at the PA site
112 and in skeletal muscle (3/14) and skin (2/14) adjacent to the PA site. *NF1* biallelic inactivation was not
113 detected in blood or IC. Of note, 2 *NF1* hits were detected in patients with *NF1*-related CPT as well as
114 patients with isolated CPT, revealing that most CPTs are caused by *NF1* loss of function (Figure 1D).
115 We observed the same *NF1* second hit in tibia and fibula in 4/5 patients affected by combined tibia and
116 fibula CPT (Figure S1A). Moreover, in 3 patients, we identified the same *NF1* second hit in PA
117 periosteum, muscle and skin surrounding the PA site (Figure S1B). These results indicate that the
118 second mutational event occurred during early skeletogenesis and was not restricted to the skeletal
119 lineage. Next, we sought to identify the cell types carrying *NF1* biallelic inactivation in the periosteum.
120 We detected 2 *NF1* hits in cultured periosteal SSPCs (pSSPCs) from 9 of the 13 patients carrying 2 hits
121 in the periosteum (Figure 1E, Table S1). Thus, pSSPCs carry *NF1* biallelic inactivation but are not the
122 only affected cell type. We then performed droplet digital PCR on sorted cell populations from PA
123 periosteum of patient P15 (Figure S1C-G). The same *NF1* variants were detected in SSPCs and in
124 Schwann cells, but not in endothelial or immune cells (Figure 1F, Figure S1E). This revealed that
125 Schwann cells also carry *NF1* biallelic inactivation in CPT, and that mutated pSSPCs and Schwann cells
126 in P15 are derived from a common lineage. *NF1* inactivation in periosteum led to an increased
127 percentage of pERK+ cells in PA compared to IC periosteum (Figure 1G). Co-immunostaining of pERK
128 and specific cell markers correlated with the genetic results as we observed the presence of increased
129 percentage of pERK+CD90+ SSPCs and pERK+SOX10+ Schwann cells in PA periosteum compared
130 to IC periosteum, but not of pERK+CD31+ endothelial cells, pERK+CD68+ immune cells, or
131 pERK+ α SMA+ pericytes/smooth muscle cells (Figure 1H). The percentages of pERK+ SSPCs and
132 Schwann cells at PA site were correlated, suggesting the presence of both mutated cell types in all
133 patients (Fig. S1H). Overall, the results show that SSPCs and Schwann cells within periosteum are the
134 cell types carrying *NF1* biallelic inactivation in CPT and that mutated pSSPCs and Schwann cells share
135 a common origin.

136

137 ***Nf1* inactivation in BC-derived pSSPCs and Schwann cells cause tibial pseudarthrosis in mice**

138 To explore the role of SSPCs and SCs in CPT, we analyzed the *Prss56-Nf1* KO mouse model (24).
139 Lineage tracing analyses in *Prss56^{Cre}; R26^{tdTom}* mice showed that BC-derived tdTom⁺ cells are a rare
140 cell population in adult bone found predominantly within the periosteum in uninjured tibia and correspond
141 to Platelet-Derived Growth Factor Receptor α ⁺ (PDGFR α ⁺) SCA1⁺ pSSPCs and SOX10⁺ Schwann
142 cells (Figure 2A, Figure S2-S3). Analyses from developmental stages to adulthood showed that *Prss56*
143 expression was not detected in bone, indicating the BC-origin of tdTom⁺ SSPCs and SCs in the
144 periosteum of *Prss56^{Cre}; R26^{tdTom}* mice (Figure S4). To determine if *Prss56-Nf1* KO mice exhibit
145 congenital pseudarthrosis, we analyzed their bone parameters and induced tibial fracture in 3-month-
146 old *Prss56^{Cre}; R26^{tdTom}; Nf1^{fl/fl}* (*Prss56-Nf1^{fl/fl}*) and *Prss56^{Cre}; R26^{tdTom}; Nf1^{fl/-}* (*Prss56-Nf1^{fl/-}*) mutant mice,
147 and *Prss56^{Cre}; R26^{tdTom}; Nf1^{+/+}* (*Prss56-Nf1^{+/+}*) controls. Although we only detected a mild reduction in
148 tibial length of uninjured tibia (Figure S5), we observed a severe reduction in callus and bone volumes
149 in both *Prss56-Nf1^{fl/fl}* and *Prss56-Nf1^{fl/-}* mutant mice through all stages of bone repair, as well as delayed
150 cartilage formation and resorption (Figure S6A-B). From day 14 post-fracture, we observed persistence
151 of fibrotic tissue in the callus (Figure 2B, Figure S6A). Absence of bone bridging was striking 28 days
152 post-fracture on microCT scans of *Prss56-Nf1^{fl/fl}* and *Prss56-Nf1^{fl/-}* mutant calluses and correlated with
153 fibrotic accumulation (Figure 2C-D, Figure S6). The percentage of bone union was significantly different
154 between mutant and control mice (p=0.0067) but not between the mutant groups (p=0.52). We
155 confirmed the fracture nonunion phenotype of *Prss56-Nf1* KO mice using a semi-stabilized fracture
156 model (Figure S7). Thus, *Nf1* biallelic inactivation in BC-derived pSSPCs and SCs leads to tibial
157 pseudarthrosis.

158

159 ***Nf1*-deficient BC-derived pSSPCs and Schwann cells contribute to callus fibrosis**

160 We then investigated the identity and fate of BC derivatives in uninjured tibia and fracture callus of
161 *Prss56-Nf1^{+/+}* and *Prss56-Nf1^{fl/fl}* mice. We observed an increased percentage of tdTom⁺ periosteal cells
162 in *Prss56-Nf1^{fl/fl}* mice compared to control mice, likely due to their increased proliferation. At 14 days
163 post-injury, tdTom⁺ cells were heterogeneously distributed in the fracture callus with regions rich in
164 tdTom⁺ cells and regions without tdTom⁺ cells (Figure S8A-B). In *Prss56-Nf1^{+/+}* control mice, tdTom⁺
165 cells were SOX9⁺ cartilage cells and OSX⁺ bone cells but their contribution to cartilage was decreased

166 in *Prss56-Nf1^{fl/fl}* mice (Figure 2E-F, Figure S8C-D). TdTom+ cells were localized in POSTN+ fibrotic
167 tissue of *Prss56-Nf1^{fl/fl}* calluses and corresponded to SOX10+ Schwann cells and *Postn*-expressing
168 fibroblastic cells (Figure 2G, Figure S8E). TdTom+ Schwann cells in callus fibrosis presented a repair
169 Schwann cell phenotype as they were positive for the stemness marker SOX2, were negative for the
170 differentiation marker Myelin Basic Protein (MBP) and were not localized along nerves (Figure 2G).
171 Although we detected tdTom+ fibrotic cells, the fibrous tissue of *Prss56-Nf1^{fl/fl}* calluses was mostly
172 composed of non-traced cells, indicating that wild-type cells also contributed to callus fibrosis (Figure
173 S8E). This correlated with NGS results from patient samples, where we observed absence or low
174 percentage of *NF1*-mutated cells in PA fibrous tissue whereas a high percentage of *NF1* mutated cells
175 was detected in PA periosteum (Table S2). Hence, *Nf1*-deficient SSPC and SCs from the periosteum,
176 as well as wild-type cells contribute to callus fibrosis in CPT.

177

178 ***NF1*-deficient periosteal SSPCs adopt a fibrotic fate during bone repair**

179 To explore the impact of *NF1* biallelic loss on the periosteum and pSSPCs, we compared PA periosteum
180 from patients P5 and P13 with IC periosteum from patients P13 and P15 using single-nucleus RNAseq
181 (snRNAseq) analyses (Figure 3A, Figure S9A-D). We identified 4 main cell populations:
182 pericytes/smooth muscle cells (SMCs), endothelial cells, immune cells, and SSPCs/fibroblasts
183 encompassing three subpopulations expressing *PDGFRA*, *ADAM12/NCAM1* (CD56), and
184 osteochondral genes (Figure 3B-C, Figure S9D). The percentage of SSPCs/fibroblasts and *ADAM12*+
185 cells was increased in periosteum from PA site (Figure 3D). In addition, PA periosteum displayed
186 increased fibrotic, osteogenic, chondrogenic, and cellular responses to TGF β lineage scores compared
187 to IC periosteum, revealing the pro-fibrotic phenotype of pSSPCs in PA periosteum (Figure 3E). We also
188 observed increased MAPK activation lineage score in PA periosteum, correlated with biallelic *NF1* loss
189 detected in this tissue. We performed bulk RNAseq analyses of IC and PA primary pSSPCs carrying
190 *NF1* biallelic inactivation and MAPK overactivation (Figure S10E). We confirmed the pro-fibrotic
191 phenotype of PA pSSPCs, which overexpressed fibrotic and MAPK-related genes and were enriched
192 for Gene Ontology related to skeletal development and extracellular matrix (ECM) (Figure S10F-G). We
193 observed increased proliferation and impaired in vitro chondrogenic differentiation (5/6 patients) of PA
194 compared to IC pSSPCs (Figure S10H-I) and detected variable effect of *NF1* biallelic inactivation on the
195 osteogenic and adipogenic differentiation of pSSPCs (Figure S10I). To investigate the impact of *NF1*

196 loss of function on the regenerative potential of pSSPCs, we grafted PA- or IC-derived pSSPCs at the
197 fracture site of immunodeficient mice (Figure 3F, Figure S10J). PA-derived pSSPCs switched from a
198 chondrogenic to a fibrotic fate after fracture as they were detected within fibrotic tissue, whereas IC-
199 derived pSSPCs mostly contributed to cartilage in the fracture callus (Figure 3G). The pro-fibrotic fate
200 of PA-derived pSSPCs led to an increase of total callus fibrosis and altered bone healing at 28 days
201 post-injury (Figure 3H). We also observed the fibrotic fate of *Nf1*-deficient pSSPCs in *Prss56-Nf1* KO
202 mice. We grafted periosteum or cultured pSSPCs from *Prss56-Nf1^{fl/fl}* mutant or *Prss56-Nf1^{+/+}* control
203 mice at the fracture site of wild-type hosts (Figure 3I, Figure S11A-G). Although the contribution to the
204 callus was equivalent (Figure S11H), we observed a reduced contribution to cartilage of mutant
205 compared to control tdTom⁺ periosteum or pSSPCs. These tdTom⁺ mutant cells were present in callus
206 fibrosis, indicating a fate change of *Nf1*-deficient pSSPCs during bone repair (Figure 3I). In sum, *NF1*
207 biallelic inactivation causes fibrotic differentiation of pSSPCs in response to bone fracture.

208

209 **Fibrotic differentiation of *Nf1*-deficient pSSPCs is due to over activation of MAPK pathway**

210 To uncover the molecular mechanisms underlying pSSPC fate conversion, we first investigated the role
211 of the MAPK pathway during the early response of pSSPCs to bone fracture. We analyzed snRNAseq
212 datasets from uninjured periosteum, and from injured periosteum and hematoma/callus at days 3, 5 and
213 7 post-fracture in wild-type mice (16) (Fig 4A). SSPCs activate in 3 successive phases: a
214 stem/progenitor phase predominant in the uninjured dataset, an injury-induced fibrogenic phase
215 predominant at day 5 post-fracture, and a bifurcation between osteogenesis and chondrogenesis,
216 predominant at day 7 post-fracture (Figure 4B). We assessed the MAPK pathway activation during these
217 3 phases using a MAPK score based on the expression profile of MAPK target genes. Along
218 pseudotime, we observed an increase of MAPK score between the SSPC and fibrogenic stages,
219 followed by a decrease when cells engage into osteochondral lineage (Figure 4C). MAPK score was
220 reduced in cells with high chondrogenic lineage score and *Sox9* expression but remained constant in
221 cells with a high osteogenic lineage score (Figure 4D). This showed that pSSPCs specifically
222 downregulate the MAPK pathway to transition from the fibrogenic to the chondrogenic stage. Co-
223 immunostaining for the chondrogenic marker SOX9 and pERK on day 7 wild-type callus sections
224 confirmed a negative correlation between SOX9 and pERK signals (Figure 4E). Analyses in tdTom⁺
225 cells showed higher pERK and reduced SOX9 signals in *Prss56-Nf1^{fl/fl}* compared to *Prss56-Nf1^{+/+}*

226 calluses. In tdTom+ *Prss56-Nf1^{+/+}* cells, we observed a negative correlation between pERK and SOX9
227 signals whereas tdTom+ *Prss56-Nf1^{fl/fl}* cells only exhibited high pERK and low SOX9 signals (Figure
228 4F). The fibrotic fate of *Nf1*-deficient pSSPCs is therefore caused by overactivation of MAPK signaling,
229 which prevents the transition from fibrogenic to chondrogenic stage required for callus formation.

230

231 ***Nf1*-deficient Schwann cells are the main driver of fibrosis in CPT**

232 Because the fibrotic tissue at the pseudarthrosis site was also composed of wild-type cells in both
233 patients with CPT and *Prss56-Nf1* KO mice, we explored the role of the mutant fracture environment on
234 SSPC fate. Transplanted wild-type GFP+ pSSPCs became fibrotic in the callus of *Prss56-Nf1^{fl/fl}* but not
235 *Prss56-Nf1^{+/+}* hosts (Figure S11I), showing the pro-fibrotic influence of the mutant callus environment.
236 We investigated the role of *Nf1*-deficient pSSPCs and SCs in this deleterious paracrine effect. Although
237 transplanted *Nf1*-deficient pSSPCs induced callus fibrosis in wild-type hosts, this fibrotic tissue was
238 resorbed, and bone bridging was apparent by 28 days post-fracture (Figure S11F-G). In contrast,
239 transplantation of *Nf1*-deficient Schwann cells at the fracture site of wild-type hosts induced tibial
240 pseudarthrosis with absence of bone bridging and fibrous accumulation at both 14 and 28 days post-
241 fracture (Figure 5A). *Nf1*-deficient Schwann cells are therefore the main driver of fibrotic accumulation
242 in tibial pseudarthrosis. We generated snRNAseq datasets of day 7 post-fracture periosteum and callus
243 of *Prss56-Nf1^{fl/fl}* mice and performed integration with day 7 control dataset (Figure 5B, Fig S12A-D).
244 Given the rarity of tdTom+ cells, *Prss56-Nf1^{fl/fl}* dataset was composed solely of non-traced (i.e., wild-
245 type) cells in mutant environment (Figure S12E). We observed a reduced proportion of cells in
246 chondrogenic clusters and increased proportion of cells in fibrogenic clusters in mutant compared to
247 control dataset (Figure 5C-D). This indicated that wild-type pSSPCs in the mutant environment are partly
248 retained in the fibrogenic stage.

249 We sought to identify the factors driving the pro-fibrotic effect of *Nf1*-deficient Schwann cells on SSPCs.
250 We observed that tdTom+ Schwann cells in the fibrotic tissue of *Prss56-Nf1^{fl/fl}* mice expressed *Tgfb1*,
251 Oncostatin M (*Osm*) and *Pdgfa* (Fig. 5E), factors previously shown to be secreted by repair SCs during
252 tissue repair (35, 36). In depth analyses of cluster 6 from the snRNAseq data, corresponding to pSSPCs
253 transitioning from the fibrogenic to the chondrogenic stage, showed an upregulation of GO terms related
254 to TGFβ specifically in *Prss56-Nf1^{fl/fl}* dataset (Figure S13). This correlated with increased *Tgfb1*
255 expression and an increased percentage of phospho-SMAD2 (TGFβ downstream effector)-positive cells

256 in day 7 *Prss56-Nf1^{fl/fl}* compared to *Prss56-Nf1^{+/+}* calluses (Figure 5F-G). To confirm the role of TGFβ
257 in the pro-fibrotic effect of *Nf1*-deficient Schwann cells, we treated wild-type mice grafted with tdTom+
258 *Prss56-Nf1^{fl/fl}* Schwann cells or *Prss56-Nf1^{fl/fl}* mice with TGFβ blocking antibody (Figure 5H). We
259 observed decreased fibrosis in the callus of treated compared to control mice. *Prss56-Nf1^{fl/fl}* mice treated
260 with TGFβ blocking antibody exhibited bone bridging and improved union score at day 28 post-fracture
261 (Figure 5I), indicating that TGFβ is one of the factors mediating the pro-fibrotic effect of *Nf1*-deficient
262 Schwann cells in tibial pseudarthrosis.

263

264 **Combined MEK and SHP2 inhibition prevents tibial pseudarthrosis**

265 To develop therapeutic approaches for CPT, we aimed to reduce the pro-fibrotic effects of *NF1* mutant
266 pSSPCs and SCs by inhibiting RAS-MAPK overactivation. We tested the efficacy of MEK inhibition using
267 selumetinib, SHP2 inhibition using SHP099, and the combination of MEK and SHP2 inhibitors to block
268 RAS-MAPK overactivation and prevent CPT. We first tested the impact of MEK with or without SHP2
269 inhibition on MAPK activation in *NF1*-deficient pSSPCs from patients with CPT. We observed a
270 substantial reduction of MAPK activation from 1 μM with combined treatment but not with single
271 treatment compared to DMSO-treated cells (Fig 6A-B). Combined MEK-SHP2 inhibition significantly
272 reduced in vitro proliferation and increased chondrogenic differentiation of *NF1*-deficient pSSPCs
273 compared to DMSO-treated cells (Figure 6C-D). As *Prss56-Nf1* KO mice faithfully recapitulate the bone
274 repair defect observed in CPT, we tested the benefit of MEK-SHP2 inhibition on this relevant preclinical
275 model of CPT by treating daily *Prss56-Nf1^{fl/-}* mice with selumetinib, SHP099, combined selumetinib and
276 SHP099, or vehicle (Figure 6E). Whereas control mice did not show bone union, mice treated with
277 combined selumetinib and SHP099 displayed an 83% union rate (Figure 6F-G), demonstrating
278 treatment efficacy in preventing pseudarthrosis. Selumetinib treatment alone had a mild effect on union
279 rate and SHP099 treatment alone was not as efficient as combined treatment (25% and 60% of union
280 rate respectively, Figure 6G). Combined MEK-SHP2 inhibition was the only treatment leading to
281 increased callus, cartilage, and bone formation and reduced fibrosis accumulation (Figure 6H).
282 Furthermore, analysis of tdTom+ cells in the fracture callus showed that combined treatment corrects
283 *Nf1*-deficient cell fate impairment, as tdTom+ cells formed cartilage instead of fibrosis in *Prss56-Nf1*
284 mutant mice treated with both SHP099 and selumetinib compared to untreated mutant mice (Figure 6I).
285 We confirmed that the combined treatment was also efficacious in the *Prx1-Nf1* KO model, in which the

286 pseudarthrosis phenotype results from *Nf1* inactivation in all pSSPCs (Fig. S14). Overall, combined
287 MEK-SHP2 inhibition efficiently prevented fibrous accumulation and pseudarthrosis, demonstrating its
288 promising therapeutic potential.

289 **Discussion**
290

291 In this study, we uncover the cellular origin and underlying molecular mechanisms of CPT,
292 demonstrating that SSPCs and Schwann cells are the affected cell types in CPT. We detected *NF1*
293 biallelic inactivation in SSPCs and Schwann cells and increased numbers of pERK+ SSPCs and
294 Schwann cells in pathological periosteum of patients with CPT. These findings correlate with the
295 presence of *Nf1*-deficient SSPCs and Schwann cells in the periosteum and fibrous callus of *Prss56-Nf1*
296 *KO* mice that exhibit tibial pseudarthrosis. Functionally, human and murine *NF1*-deficient pSSPCs in
297 both *Prss56-Nf1* *KO* and *Prx1-Nf1* *KO* mouse models displayed a pro-fibrotic phenotype and contributed
298 to callus fibrosis. The role of MAPK signaling in regulating SSPC differentiation is unclear, as previous
299 studies showed beneficial and deleterious effect of MAPK cascade in chondrogenesis (37–42). Using
300 snRNAseq, we established the temporal dynamics of MAPK signaling required during pSSPC activation
301 and differentiation in response to fracture. MAPK signaling is first up-regulated in pSSPCs that transition
302 from a stem/progenitor stage to an injury-induced fibrogenic stage and is down-regulated during the
303 transition from fibrogenesis to chondrogenesis. These results provide the molecular mechanism
304 explaining the retention of *NF1*-deficient pSSPCs in the fibrogenic state as they fail to downregulate
305 MAPK signaling due to *NF1* loss of function. Consequently, fibrotic pSSPCs accumulate in the center
306 of the callus and interfere with fracture consolidation. These results may have a broader impact in
307 understanding other fibrotic bone repair disorders sharing similar mechanisms with CPT.

308
309 Most strikingly, we demonstrate that *NF1* biallelic inactivation in CPT is not restricted to the skeletal
310 lineage. Our results highlight the pivotal role of Schwann cells (SCs), a neural cell type, in promoting
311 callus fibrosis in CPT. We identified *NF1*-deficient SCs as the source of pro-fibrotic factors causing tibial
312 pseudarthrosis in *Prss56-Nf1* *KO* mice. Although *Nf1*-deficient pSSPCs exert a pro-fibrotic effect, SCs
313 are the main fibrotic drivers in CPT recruiting wild type pSSPCs to contribute also to callus fibrosis. SCs
314 in the fibrous callus of *Prss56-Nf1* *KO* mice exhibit a repair SC phenotype. Previous studies showed that
315 MAPK pathway regulates the transition from SCs to repair SCs suggesting that *Nf1*-deficient SCs are
316 blocked in a repair SC state and maintain the secretion of pro-fibrotic factors in CPT (43–45). We
317 identified that *Nf1*-deficient SCs express several profibrotic factors including TGF β , OSM, and PDGF-
318 AA and that inhibiting TGF β improved healing in *Prss56-Nf1* *KO* mice. This study provides evidence
319 that SCs can interfere with the repair process of non-peripheral nervous tissues and promote fibrotic

320 tissue accumulation. Whereas previous studies highlighted the key paracrine role of SCs in skin and
321 digit tip regeneration, the involvement of SCs and peripheral nerves in tissue repair dysfunctions and
322 fibrotic disorders remains understudied (35, 36, 46).

323

324 The involvement of both pSSPCs and SCs in CPT reveals mechanisms for NF1 bone manifestations.
325 CPT and other NF1 bone phenotypes have been investigated independent of other NF1 symptoms,
326 presumably because the cell types involved have distinct embryonic origins. SCs and melanocytes,
327 responsible for NFBs and CALMs, are neural crest-derived, whereas axial and appendicular bones are
328 derived from the mesoderm. Our genetic analysis of the *NF1* mutational landscape in CPT revealed that
329 *NF1* 2nd hit occurs early during embryonic development and is not restricted to the skeletal lineage. In
330 addition, we detected the same 2 *NF1* hits in SSPCs and SCs in pathological periosteum of one patient
331 with CPT, showing that both affected cell types share a common origin. In mice, we identified BCs as a
332 population giving rise to SCs and pSSPCs in long bones and showed that *Nf1* loss in these derivatives
333 cause pseudarthrosis. This shows that BCs are the cellular origin of CPT in mice, and presumably in
334 NF1 patients. The *Prss56-Nf1* KO model is the first relevant model to faithfully recapitulate the variability
335 of NF1 symptoms, demonstrating that CPT shares a common BC origin with NFBs and CALMs (24). In
336 addition to sharing a common cellular origin, we further reveal that CPTs and NFBs share common
337 pathogenic mechanisms. In NFBs, *Nf1*-deficient SCs also secrete profibrotic factors, including TGF β
338 and SCF, to promote fibroblast accumulation and proliferation involved in tumor progression (47–49).
339 Our study thus highlights the parallels between NF1 symptoms and calls for more integrated analysis of
340 NF1 features.

341

342 Beside unraveling the pathogenic bases of CPT, we demonstrate the relevance of the *Prss56-Nf1* KO
343 mouse model as a preclinical model for CPT-related fibrous nonunion. Because NF1 symptoms share
344 common pathogenic mechanisms, we considered therapeutical strategies developed for tumoral
345 manifestations and showed that they can also be considered for CPT treatment. Selumetinib is FDA-
346 approved for inoperable neurofibroma yet did not reveal substantial effects in previous mouse models
347 of NF1 bone manifestations (19, 32, 50). Therefore, we tested the combination of MEK and SHP2
348 inhibitors to counteract the pro-fibrotic effects of *NF1*-deficient pSSPCs and SCs. We observed a
349 therapeutic effect of the selumetinib/SHP099 combination with efficient MAPK inhibition in *NF1*-deficient

350 pSSPCs and restoration of the in vitro proliferation and differentiation potential of human pSSPCs. In
351 vivo treatment of *Prss56-Nf1* KO or *Prx1-Nf1* KO mice showed promising results, with bone union
352 reached in 83% and 100% of callus respectively, concomitant with a drastic decrease in fibrotic
353 accumulation one month after fracture. The effect of a 10-day oral treatment opens the door to clinical
354 strategies for CPT overcoming potential tolerability issues of combining SHP2 and MEK inhibitors. In
355 addition, the possibility of using local delivery to minimize these issues could also be tested. These
356 results represent a potential breakthrough in improving the prognosis for CPT patients.

357

358 There are limitations to this study. CPT is extremely rare (1/150 000 individuals) and patients undergo
359 surgical treatment at a young age (first surgery at 3.1 ± 1 years-old). Thus, obtaining periosteum samples
360 of patients with CPT is challenging and only small amounts of tissues can be collected. This strongly
361 limits our ability to isolate rare cell populations, including SCs, for extensive analysis. Similarly, in
362 *Prss56-Nf1* KO mice, BC derivatives represent a rare subset of cells in intact periosteum and in the
363 callus after fracture. This highlights the strong paracrine effect of *Nf1*-deficient cells but makes it
364 challenging to isolate BC-derived cells to further explore the impact of *Nf1* loss of function in these cells.
365 Last, the *Prss56-Nf1* KO mouse model recapitulates the fibrous nonunion phenotype, but not congenital
366 tibial bowing, which might suggest independent mechanisms and require further studies.

367 **Materials and Methods**

368

369 **Study design**

370 In our study, we aimed to understand the mechanisms causing CPT. We combined the analyses of
371 samples from patients undergoing surgery for CPT with the analyses of the relevant *Prss56-Nf1* KO
372 mouse model. For the human cohort, we collected tissues from patients operated for CPT at Necker-
373 Enfants Malades hospital during this study and formal consent was obtained. For each patient, the
374 affected PA tissue was compared with non-affected IC tissue. Two patients undergoing reintervention
375 were excluded from the cohort as original PA tissues from the first resection were not accessible and
376 we did not detect *NF1* biallelic inactivation. Therefore, we could not conclude on the presence/absence
377 of *NF1* mutation. For the mouse study, all animals used for the study were included except samples with
378 distal or proximal fractures that can affect bone repair. No outliers were excluded from the study. Based
379 on our previous publications (12, 13, 51), groups of 3 to 7 samples are sufficient to assess statistical
380 differences between groups. The n for individual experiments is indicated in the figure legends. Every
381 group is composed of samples from at least 2 independent experiments. For both human and mouse
382 studies, samples were assigned a unique sample number for blinded analyses. No randomization
383 methods were used for the study, as groups were homogeneous and composed of equivalent animals
384 based on gender, age, and genotype.

385

386 **Human tissue sample collection**

387 *Cohort and ethical approval*

388 Sample collection from patients affected by congenital pseudarthrosis of the tibia (CPT) was performed
389 at Necker-Enfants Malades Hospital, Paris. This study was approved by the Ethics Committee CPP-
390 IDF-2 (#ID-RCB/EUDRACT: 2014- A01420-47; IMNIS2014-03). Informed consent of legal
391 representatives of patients was obtained prior to sample collection. The cohort was composed of 17
392 patients, 7 diagnosed with *NF1*-associated CPT and 10 with isolated CPT. *NF1* diagnosis was
393 performed by the Dermatology department at Necker-Enfants Malades Hospital, following guidelines
394 from International Consensus Group on Neurofibromatosis Diagnostic Criteria. Isolated CPT was
395 defined by the absence of additional *NF1* clinical feature and the absence of *NF1* pathogenic variant in
396 blood sample. 14 patients were treated for the first time (named “Primary” operation in Table S1) and 3

397 were undergoing additional surgery following initial treatment (named “Reintervention”). Detailed
398 information about patient age, gender, NF1 diagnosis, type of operation and affected bones are reported
399 in Table S1.

400

401 *Sample collection*

402 Tissues were collected during CPT treatment surgery using the induced membrane technique typically
403 performed in 2 steps (52). The first surgical procedure consists of pseudarthrosis tissue resection,
404 intramedullary nailing, and insertion of a cement spacer to fill the gap. During this procedure, affected
405 periosteum, bone marrow, bone, fibrous tissue, muscle, and skin from the PA site were collected. For
406 patients undergoing surgery as secondary treatment, the primary pseudarthrosis tissues were
407 unavailable but were collected adjacent to the primary PA site when possible. After 6 to 8 weeks, a
408 second surgical procedure was performed to remove the cement spacer and graft autologous iliac crest
409 periosteum and cancellous bone in the induced membrane that formed around the cement. During this
410 second procedure, unaffected periosteum and spongy bone from the iliac crest (IC) were harvested. A
411 blood sample was also collected during surgery. Tissue dissection and identification was performed by
412 orthopedic surgeons. Collected tissues were immediately placed in DMEM (21063029, ThermoFischer
413 Scientific) with 10% HEPES (15630056, ThermoFischer Scientific) and 1% Penicillin-Streptomycin
414 (15140122, ThermoFischer Scientific) at 4°C, and processed for *NF1* genotyping, single-nuclei RNAseq,
415 primary culture and histological analyses as described below.

416

417 **Mice**

418 C57BL/6ScNj, *Prx1^{Cre}* (IMSR_JAX:005584) (53), *Rosa26-mtdTomato-mEGFP* (*R26^{mTmG}*)
419 (IMSR_JAX:007676) (54), *R26tdTomato* (*R26^{tdTom}*) (IMSR_JAX:007914) (55), *Nf1^{flox}* (*Nf1^{fl}*)
420 (IMSR_JAX:017640), *Nf1*-knock out (*Nf1⁻*) (56) were obtained from Jackson Laboratory. *Prss56^{Cre}* mice
421 were generated by Piotr Topilko (24, 25). Immunodeficient nude CD1 mice were purchased from Janvier
422 Labs. Mice were bred in animal facilities at IMRB, Creteil and Imagine Institute, Paris. Two to five mice
423 were kept in separated ventilated cages, in a pathogen-controlled environment with 12:12-hour
424 light:dark cycles and ad libitum access to water and food. All procedures performed were approved by
425 Paris University or Paris Est Creteil University Ethical Committees (#2795-201506051048131, #19295-
426 2019052015468705, #27181-202009141201846, #33818-2021110818301267). Males and females

427 were mixed in experimental groups. No specific randomization method was used. Bone injury and tissue
428 collection for graft and digestion were performed on 10- to 14-week-old mice. Six- to 8-week-old mice
429 were used for primary periosteum culture. Controlled breeding was performed to collect embryonic
430 tissues at 12.5, 13.5, and 14.5 days of development. Samples were labeled at the time of tissue
431 collection and using a labeling system allowing blind analyses in all experiments.

432

433 **Statistical analyses**

434 Data are reported as mean +/- standard deviation. n represents the number of samples used for the
435 analysis. For human experiments, each sample corresponds to a different patient. For mouse
436 experiments, each sample corresponds to an individual mouse. Statistical differences between
437 experimental groups were evaluated using GraphPad Prism. For comparison between 2 groups, two-
438 side Mann-Whitney test was used. For comparison between 3 or 4 groups, one-way ANOVA followed
439 by Holm-Šídák's multiple comparisons post-hoc test was used. The comparison in bone bridging
440 between mutants and control groups was performed using Chi-squared test. For SOX9/pERK signal
441 correlation, each value corresponds to an individual cell. Correlation analysis and simple linear
442 regression were performed to assess the correlation between both signals. Significance was determined
443 as *p < 0.05, **p < 0.01, ***p < 0.001, ****p < 0.0001. All experiments were performed in at least 2
444 independent experiments.

445

446 **List of Supplementary Materials**

447

448 Material and Methods

449 Figure S1 to Figure S14

450 Table S1 to Table S6

451 MDAR checklist

452 Data File S1

453 **References**

- 454 1. S. Pannier, Congenital pseudarthrosis of the tibia. *Orthopaedics & Traumatology: Surgery & Research*
455 **97**, 750–761 (2011).
- 456 2. M. J. Siebert, C. A. Makarewich, Anterolateral Tibial Bowing and Congenital Pseudoarthrosis of the
457 Tibia: Current Concept Review and Future Directions. *Curr Rev Musculoskelet Med* **15**, 438–446 (2022).
- 458 3. D. H. Gutmann, R. E. Ferner, R. H. Listernick, B. R. Korf, P. L. Wolters, K. J. Johnson,
459 Neurofibromatosis type 1. *Nat Rev Dis Primers* **3**, 17004 (2017).
- 460 4. I. Eisenbarth, G. Assum, D. Kaufmann, W. Krone, Evidence for the presence of the second allele of
461 the neurofibromatosis type 1 gene in melanocytes derived from café au lait macules of NF1 patients.
462 *Biochem Biophys Res Commun* **237**, 138–141 (1997).
- 463 5. L. Kluwe, R. Friedrich, V. F. Mautner, Loss of NF1 allele in Schwann cells but not in fibroblasts derived
464 from an NF1-associated neurofibroma. *Genes Chromosomes Cancer* **24**, 283–285 (1999).
- 465 6. L. Q. Le, C. Liu, T. Shipman, Z. Chen, U. Suter, L. F. Parada, Susceptible stages in Schwann cells
466 for NF1-associated plexiform neurofibroma development. *Cancer Res* **71**, 4686–4695 (2011).
- 467 7. J. Wu, J. P. Williams, T. A. Rizvi, J. J. Kordich, D. Witte, D. Meijer, A. O. Stemmer-Rachamimov, J.
468 A. Cancelas, N. Ratner, Plexiform and dermal neurofibromas and pigmentation are caused by Nf1 loss
469 in desert hedgehog-expressing cells. *Cancer Cell* **13**, 105–116 (2008).
- 470 8. Y. Zhu, P. Ghosh, P. Charnay, D. K. Burns, L. F. Parada, Neurofibromas in NF1: Schwann cell origin
471 and role of tumor environment. *Science* **296**, 920–922 (2002).
- 472 9. B. Hermanns-Sachweh, J. Senderek, J. Alfer, B. Klosterhalfen, R. Büttner, L. Füzési, M. Weber,
473 Vascular changes in the periosteum of congenital pseudarthrosis of the tibia. *Pathol Res Pract* **201**,
474 305–312 (2005).
- 475 10. D. A. Stevenson, H. Zhou, S. Ashrafi, L. M. Messiaen, J. C. Carey, J. L. D’Astous, S. D. Santora, D.
476 H. Viskochil, Double inactivation of NF1 in tibial pseudarthrosis. *Am J Hum Genet* **79**, 143–148 (2006).
- 477 11. C. Brekelmans, S. Hollants, C. De Groote, N. Sohier, M. Maréchal, L. Geris, F. P. Luyten, L.
478 Ginckels, R. Sciot, T. de Ravel, L. De Smet, J. Lammens, E. Legius, H. Brems, Neurofibromatosis type
479 1-related pseudarthrosis: Beyond the pseudarthrosis site. *Hum Mutat* **40**, 1760–1767 (2019).
- 480 12. O. Duchamp de Lageneste, A. Julien, R. Abou-Khalil, G. Frangi, C. Carvalho, N. Cagnard, C.
481 Cordier, S. J. Conway, C. Colnot, Periosteum contains skeletal stem cells with high bone regenerative
482 potential controlled by Periostin. *Nat Commun* **9**, 773 (2018).
- 483 13. A. Julien, S. Perrin, E. Martínez-Sarrà, A. Kanagalingam, C. Carvalho, M. Luka, M. Ménager, C.

484 Colnot, Skeletal stem/progenitor cells in periosteum and skeletal muscle share a common molecular
485 response to bone injury. *J of Bone & Mineral Res* , jbmr.4616 (2022).

486 14. Z. Li, C. A. Meyers, L. Chang, S. Lee, Z. Li, R. Tomlinson, A. Hoke, T. L. Clemens, A. W. James,
487 Fracture repair requires TrkA signaling by skeletal sensory nerves. *Journal of Clinical Investigation* **129**,
488 5137–5150 (2019).

489 15. B. G. Matthews, S. Novak, F. V. Sbrana, J. L. Funnell, Y. Cao, E. J. Buckels, D. Grcevic, I. Kalajzic,
490 Heterogeneity of murine periosteum progenitors involved in fracture healing. *eLife* **10**, e58534 (2021).

491 16. S. Perrin, C.-A. Wotawa, V. Bretegnier, M. Luka, F. Culpier, C. Masson, M. Ménager, C. Colnot,
492 Single nuclei transcriptomics reveal the differentiation trajectories of periosteal skeletal/stem progenitor
493 cells in bone regeneration (2024), doi:10.7554/eLife.92519.1.

494 17. N. van Gastel, S. Stegen, G. Eelen, S. Schoors, A. Carlier, V. W. Daniëls, N. Baryawno, D.
495 Przybylski, M. Depypere, P.-J. Stiers, D. Lambrechts, R. Van Looveren, S. Torrekens, A. Sharda, P.
496 Agostinis, D. Lambrechts, F. Maes, J. V. Swinnen, L. Geris, H. Van Oosterwyck, B. Thienpont, P.
497 Carmeliet, D. T. Scadden, G. Carmeliet, Lipid availability determines fate of skeletal progenitor cells via
498 SOX9. *Nature* **579**, 111–117 (2020).

499 18. J. Sales de Gauzy, F. Fitoussi, J.-L. Jouve, C. Karger, A. Badina, A.-C. Masquelet, Traumatic
500 diaphyseal bone defects in children. *Orthopaedics & Traumatology: Surgery & Research* **98**, 220–226
501 (2012).

502 19. J. de la Croix Ndong, D. M. Stevens, G. Vignaux, S. Uppuganti, D. S. Perrien, X. Yang, J. S. Nyman,
503 E. Harth, F. Elefteriou, Combined MEK Inhibition and BMP2 Treatment Promotes Osteoblast
504 Differentiation and Bone Healing in *Nf1*^{osx^{-/-}} Mice: RAS/ERK SIGNALING IN OSTEOPROGENITORS.
505 *J Bone Miner Res* **30**, 55–63 (2015).

506 20. T. El Khassawna, D. Toben, M. Kolanczyk, K. Schmidt-Bleek, I. Koennecke, H. Schell, S. Mundlos,
507 G. N. Duda, Deterioration of fracture healing in the mouse model of NF1 long bone dysplasia. *Bone* **51**,
508 651–660 (2012).

509 21. N. Kamiya, R. Yamaguchi, O. Aruwajoye, A. J. Kim, G. Kuroyanagi, M. Phipps, N. S. Adapala, J. Q.
510 Feng, H. K. Kim, Targeted Disruption of *NF1* in Osteocytes Increases FGF23 and Osteoid With
511 Osteomalacia-like Bone Phenotype: NF1 DISRUPTION IN OSTEOCYTES CAUSES A
512 MINERALIZATION DEFECT. *J Bone Miner Res* **32**, 1716–1726 (2017).

513 22. R. Sharma, X. Wu, S. D. Rhodes, S. Chen, Y. He, J. Yuan, J. Li, X. Yang, X. Li, L. Jiang, E. T. Kim,

514 D. A. Stevenson, D. Viskochil, M. Xu, F.-C. Yang, Hyperactive Ras/MAPK signaling is critical for tibial
515 nonunion fracture in neurofibromin-deficient mice. *Human Molecular Genetics* **22**, 4818–4828 (2013).

516 23. W. Wang, J. S. Nyman, K. Ono, D. A. Stevenson, X. Yang, F. Elefteriou, Mice lacking Nf1 in
517 osteochondroprogenitor cells display skeletal dysplasia similar to patients with neurofibromatosis type
518 I. *Human Molecular Genetics* **20**, 3910–3924 (2011).

519 24. K. J. Radomska, F. Couplier, A. Gresset, A. Schmitt, A. Debbiche, S. Lemoine, P. Wolkenstein, J.-
520 M. Vallat, P. Charnay, P. Topilko, Cellular Origin, Tumor Progression, and Pathogenic Mechanisms of
521 Cutaneous Neurofibromas Revealed by Mice with Nf1 Knockout in Boundary Cap Cells. *Cancer Discov*
522 **9**, 130–147 (2019).

523 25. A. Gresset, F. Couplier, G. Gerschenfeld, A. Jourdon, G. Matesic, L. Richard, J.-M. Vallat, P.
524 Charnay, P. Topilko, Boundary Caps Give Rise to Neurogenic Stem Cells and Terminal Glia in the Skin.
525 *Stem Cell Reports* **5**, 278–290 (2015).

526 26. S. Ahsan, Y. Ge, M. A. Tainsky, Combinatorial therapeutic targeting of BMP2 and MEK-ERK
527 pathways in NF1-associated malignant peripheral nerve sheath tumors. *Oncotarget* **7**, 57171–57185
528 (2016).

529 27. E. Dombi, A. Baldwin, L. J. Marcus, M. J. Fisher, B. Weiss, A. Kim, P. Whitcomb, S. Martin, L. E.
530 Aschbacher-Smith, T. A. Rizvi, J. Wu, R. Ershler, P. Wolters, J. Therrien, J. Glod, J. B. Belasco, E.
531 Schorry, A. Brofferio, A. J. Starosta, A. Gillespie, A. L. Doyle, N. Ratner, B. C. Widemann, Activity of
532 Selumetinib in Neurofibromatosis Type 1-Related Plexiform Neurofibromas. *N Engl J Med* **375**, 2550–
533 2560 (2016).

534 28. D. Casey, S. Demko, A. Sinha, P. S. Mishra-Kalyani, Y.-L. Shen, S. Khasar, M. A. Goheer, W. S.
535 Helms, L. Pan, Y. Xu, J. Fan, R. Leong, J. Liu, Y. Yang, K. Windsor, M. Ou, O. Stephens, B. Oh, G. H.
536 Reaman, A. Nair, S. S. Shord, V. Bhatnagar, S. R. Daniels, S. Sickafuse, K. B. Goldberg, M. R. Theoret,
537 R. Pazdur, H. Singh, FDA Approval Summary: Selumetinib for Plexiform Neurofibroma. *Clin Cancer Res*
538 **27**, 4142–4146 (2021).

539 29. A. M. Gross, E. Dombi, P. L. Wolters, A. Baldwin, A. Dufek, K. Herrera, S. Martin, J. Derdak, K. S.
540 Heisey, P. M. Whitcomb, S. M. Steinberg, D. J. Venzon, M. J. Fisher, A. R. Kim, M. Bornhorst, B. D.
541 Weiss, J. O. Blakeley, M. A. Smith, B. C. Widemann, Long-Term Safety and Efficacy of Selumetinib in
542 Children with Neurofibromatosis Type 1 on a Phase 1/2 Trial for Inoperable Plexiform Neurofibromas.
543 *Neuro Oncol* , noad086 (2023).

- 544 30. G. S. Baht, P. Nadesan, D. Silkstone, B. A. Alman, Pharmacologically targeting beta-catenin for NF1
545 associated deficiencies in fracture repair. *Bone* **98**, 31–36 (2017).
- 546 31. N. Deo, T. L. Cheng, K. Mikulec, L. Peacock, D. G. Little, A. Schindeler, Improved union and bone
547 strength in a mouse model of NF1 pseudarthrosis treated with recombinant human bone morphogenetic
548 protein-2 and zoledronic acid: rhBMP-2 AND ZA FOR NF1 PSEUDARTHROSIS. *J. Orthop. Res.* (2017),
549 doi:10.1002/jor.23672.
- 550 32. W. Wang, J. S. Nyman, H. E. Moss, G. Gutierrez, G. R. Mundy, X. Yang, F. Elefteriou, Local low-
551 dose lovastatin delivery improves the bone-healing defect caused by Nf1 loss of function in osteoblasts.
552 *J Bone Miner Res* **25**, 1658–1667 (2010).
- 553 33. J. Cai, S. Jacob, R. Kurupi, K. M. Dalton, C. Coon, P. Greninger, R. K. Egan, G. T. Stein, E. Murchie,
554 J. McClanaghan, Y. Adachi, K. Hirade, M. Dozmorov, J. Glod, S. A. Boikos, H. Ebi, H. Hao, G.
555 Caponigro, C. H. Benes, A. C. Faber, High-risk neuroblastoma with NF1 loss of function is targetable
556 using SHP2 inhibition. *Cell Rep* **40**, 111095 (2022).
- 557 34. J. Wang, K. Pollard, A. N. Allen, T. Tomar, D. Pijnenburg, Z. Yao, F. J. Rodriguez, C. A. Pratilas,
558 Combined Inhibition of SHP2 and MEK Is Effective in Models of NF1-Deficient Malignant Peripheral
559 Nerve Sheath Tumors. *Cancer Res* **80**, 5367–5379 (2020).
- 560 35. A. P. W. Johnston, S. A. Yuzwa, M. J. Carr, N. Mahmud, M. A. Storer, M. P. Krause, K. Jones, S.
561 Paul, D. R. Kaplan, F. D. Miller, Dedifferentiated Schwann Cell Precursors Secreting Paracrine Factors
562 Are Required for Regeneration of the Mammalian Digit Tip. *Cell Stem Cell* **19**, 433–448 (2016).
- 563 36. V. Parfejevs, J. Debbache, O. Shakhova, S. M. Schaefer, M. Glausch, M. Wegner, U. Suter, U.
564 Riekstina, S. Werner, L. Sommer, Injury-activated glial cells promote wound healing of the adult skin in
565 mice. *Nat Commun* **9**, 236 (2018).
- 566 37. B. E. Bobick, W. M. Kulyk, MEK-ERK signaling plays diverse roles in the regulation of facial
567 chondrogenesis. *Exp Cell Res* **312**, 1079–1092 (2006).
- 568 38. B. E. Bobick, W. M. Kulyk, The MEK-ERK signaling pathway is a negative regulator of cartilage-
569 specific gene expression in embryonic limb mesenchyme. *J Biol Chem* **279**, 4588–4595 (2004).
- 570 39. J. Li, Z. Zhao, J. Liu, N. Huang, D. Long, J. Wang, X. Li, Y. Liu, MEK/ERK and p38 MAPK regulate
571 chondrogenesis of rat bone marrow mesenchymal stem cells through delicate interaction with TGF-
572 beta1/Smads pathway. *Cell Prolif* **43**, 333–343 (2010).
- 573 40. S. Murakami, M. Kan, W. L. McKeehan, B. de Crombrughe, Up-regulation of the chondrogenic

574 Sox9 gene by fibroblast growth factors is mediated by the mitogen-activated protein kinase pathway.
575 *Proc Natl Acad Sci U S A* **97**, 1113–1118 (2000).

576 41. C. D. Oh, S. H. Chang, Y. M. Yoon, S. J. Lee, Y. S. Lee, S. S. Kang, J. S. Chun, Opposing role of
577 mitogen-activated protein kinase subtypes, erk-1/2 and p38, in the regulation of chondrogenesis of
578 mesenchymes. *J Biol Chem* **275**, 5613–5619 (2000).

579 42. A. D. Weston, R. A. S. Chandraratna, J. Torchia, T. M. Underhill, Requirement for RAR-mediated
580 gene repression in skeletal progenitor differentiation. *J Cell Biol* **158**, 39–51 (2002).

581 43. M. C. Harrisingh, E. Perez-Nadales, D. B. Parkinson, D. S. Malcolm, A. W. Mudge, A. C. Lloyd, The
582 Ras/Raf/ERK signalling pathway drives Schwann cell dedifferentiation. *EMBO J* **23**, 3061–3071 (2004).

583 44. I. Napoli, L. A. Noon, S. Ribeiro, A. P. Kerai, S. Parrinello, L. H. Rosenberg, M. J. Collins, M. C.
584 Harrisingh, I. J. White, A. Woodhoo, A. C. Lloyd, A central role for the ERK-signaling pathway in
585 controlling Schwann cell plasticity and peripheral nerve regeneration in vivo. *Neuron* **73**, 729–742
586 (2012).

587 45. I. Cervellini, J. Galino, N. Zhu, S. Allen, C. Birchmeier, D. L. Bennett, Sustained MAPK/ERK
588 Activation in Adult Schwann Cells Impairs Nerve Repair. *J Neurosci* **38**, 679–690 (2018).

589 46. A. P. W. Johnston, S. Naska, K. Jones, H. Jinno, D. R. Kaplan, F. D. Miller, Sox2-mediated regulation
590 of adult neural crest precursors and skin repair. *Stem Cell Reports* **1**, 38–45 (2013).

591 47. A. Badache, N. Muja, G. H. De Vries, Expression of Kit in neurofibromin-deficient human Schwann
592 cells: role in Schwann cell hyperplasia associated with type 1 neurofibromatosis. *Oncogene* **17**, 795–
593 800 (1998).

594 48. G. A. Mashour, N. Ratner, G. A. Khan, H. L. Wang, R. L. Martuza, A. Kurtz, The angiogenic factor
595 midkine is aberrantly expressed in NF1-deficient Schwann cells and is a mitogen for neurofibroma-
596 derived cells. *Oncogene* **20**, 97–105 (2001).

597 49. D. M. Patmore, S. Welch, P. C. Fulkerson, J. Wu, K. Choi, D. Eaves, J. J. Kordich, M. H. Collins, T.
598 P. Cripe, N. Ratner, *In Vivo* Regulation of TGF- β by R-Ras2 Revealed through Loss of the RasGAP
599 Protein NF1. *Cancer Research* **72**, 5317–5327 (2012).

600 50. J. El-Hoss, T. Cheng, E. C. Carpenter, K. Sullivan, N. Deo, K. Mikulec, D. G. Little, A. Schindeler, A
601 Combination of rhBMP-2 (Recombinant Human Bone Morphogenetic Protein-2) and MEK (MAP
602 Kinase/ERK Kinase) Inhibitor PD0325901 Increases Bone Formation in a Murine Model of
603 Neurofibromatosis Type I Pseudarthrosis. *The Journal of Bone and Joint Surgery* **96**, e117 (2014).

604 51. A. Julien, A. Kanagalingam, E. Martínez-Sarrà, J. Megret, M. Luka, M. Ménager, F. Relaix, C. Colnot,
605 Direct contribution of skeletal muscle mesenchymal progenitors to bone repair. *Nature Communications*
606 **12**, 2860 (2021).

607 52. A. C. Masquelet, F. Fitoussi, T. Begue, G. P. Muller, [Reconstruction of the long bones by the
608 induced membrane and spongy autograft]. *Ann Chir Plast Esthet* **45**, 346–353 (2000).

609 53. M. Logan, J. F. Martin, A. Nagy, C. Lobe, E. N. Olson, C. J. Tabin, Expression of Cre recombinase
610 in the developing mouse limb bud driven by aPrxl enhancer. *genesis* **33**, 77–80 (2002).

611 54. M. D. Muzumdar, B. Tasic, K. Miyamichi, L. Li, L. Luo, A global double-fluorescent Cre reporter
612 mouse. *Genesis* **45**, 593–605 (2007).

613 55. L. Madisen, T. A. Zwingman, S. M. Sunkin, S. W. Oh, H. A. Zariwala, H. Gu, L. L. Ng, R. D. Palmiter,
614 M. J. Hawrylycz, A. R. Jones, E. S. Lein, H. Zeng, A robust and high-throughput Cre reporting and
615 characterization system for the whole mouse brain. *Nat Neurosci* **13**, 133–140 (2010).

616 56. Y. Zhu, M. I. Romero, P. Ghosh, Z. Ye, P. Charnay, E. J. Rushing, J. D. Marth, L. F. Parada, Ablation
617 of NF1 function in neurons induces abnormal development of cerebral cortex and reactive gliosis in the
618 brain. *Genes Dev* **15**, 859–876 (2001).

619

620 **Acknowledgements**

621 We thank A. Henry, A. Guigan and O. Pellé from the Flow Cytometry platforms of IMRB and Imagine
622 Institute, L. Slimani and K. Henri from Life Imaging Facility of Paris Cité University (Plateforme Imagerie
623 du Vivant “Micro-CT platform”), all the staff from the Imagine genomic core facility at Imagine Institute
624 and N. Cagnard from Bioinformatics Platform at Imagine Institute for advice and technical assistance.
625 We thank A. Julien, C. Goachet, M. Ethel, S. Berger, E. Tacu, E. Paniel, A. Heisler, and M. Mansour for
626 technical assistance or advice.

627

628 **Fundings**

629 This work was supported by
630 Association Neurofibromatoses et Recklinghausen (C.C and B.P.), Osteosynthesis and Trauma Care
631 Foundation (C.C. and St.P.), Agence Nationale de la Recherche-18-CE14-0033 and 21-CE18-007-01
632 (C.C, P.T. and B.P.), US Department of the Army NF220019 (C.C.), National Institutes of Health NIAMS
633 R01 AR081671 (C.C. and Ralph Marcucio), and IMRB Cross team award (C.C. and P.T.). S. Perrin and
634 O. Duchamp de Lageneste were supported by a PhD fellowship from Paris Cité University.

635

636 **Author contributions**

637 Si.P., C.C., P.T. and B.P. conceptualized and formulated the project. Si.P., Sa.P., I.L., V.B, O.D.d.L,
638 N.P., O.R., M.L., F.C., C.M., T.M., and M.Z. performed experiments. St.P., P.W., S.H-R., K.R., P.T. and
639 M.M. provided resources. Si.P. performed bioinformatic analyses. C.C. supervised the work. Si.P.
640 generated the figures. Si.P. and C.C. wrote the original draft of the manuscript. P.T. and B.P reviewed
641 and edited the manuscript.
642
643

644 **Competing interests**

645 The authors declare that they have no competing interests.

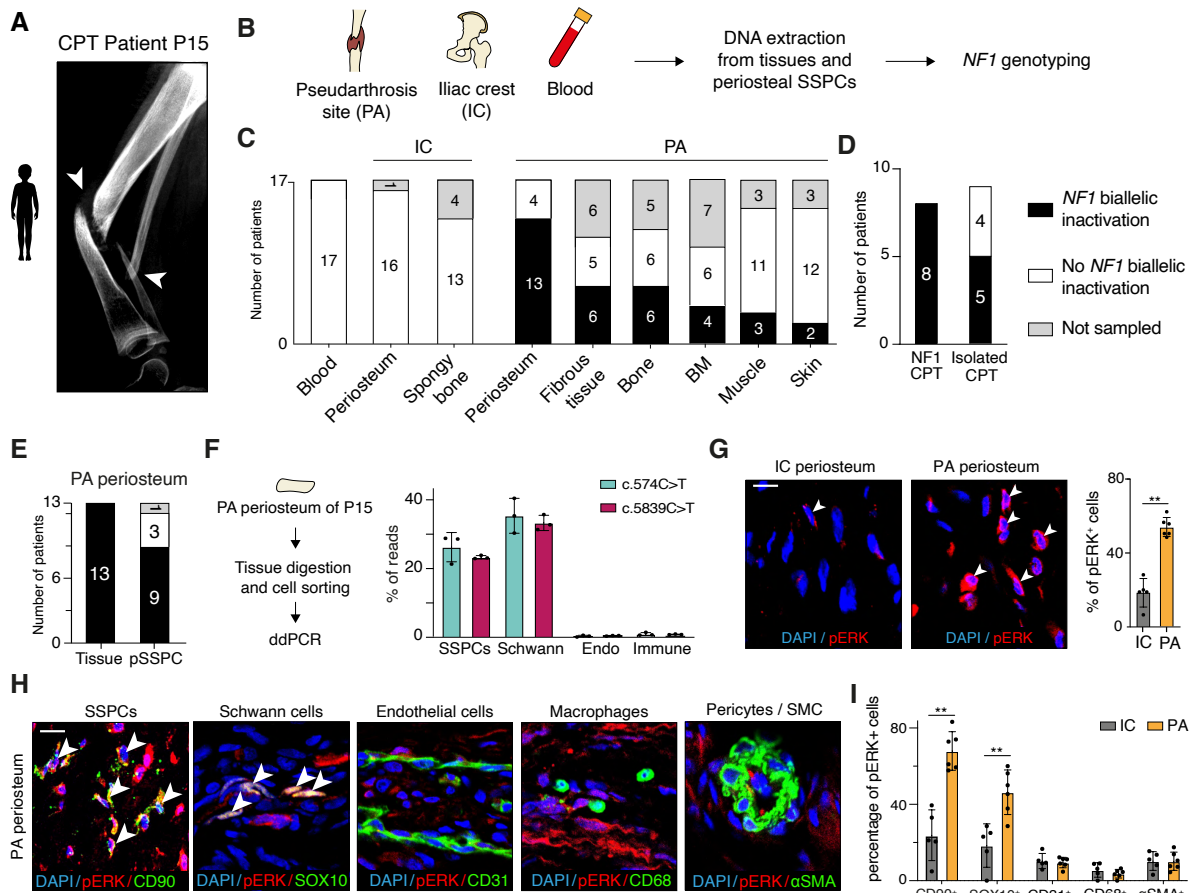
646

647 **Data and materials availability**

648 All data from this study are present in the paper or supplementary materials. Single-nuclei RNAseq
649 and bulk RNAseq datasets generated for this study are deposited in GEO (GSE232516, GSE232517,
650 GSE234071) and are publicly available.

651 **Figures**

Figure 1



652

653 **Figure 1: Schwann cells and SSPCs within periosteum harbor *NF1* biallelic inactivation in CPT**

654 **A.** X-ray of the tibia and fibula pseudarthrosis (white arrows) of patient with CPT P15. **B.** Experimental

655 design. DNA was extracted from tissues or periosteal SSPCs (pSSPCs) collected at the pseudarthrosis

656 (PA) site and the iliac crest (IC), and from blood of patients with CPT undergoing surgery, and *NF1*

657 targeted sequencing was performed. **C.** *NF1* genotyping of tissues from 17 patients with CPT shows the

658 absence of *NF1* biallelic inactivation in blood and IC and the presence of *NF1* biallelic inactivation in the

659 periosteum at PA site in 13/17 patients. *NF1* biallelic inactivation was also detected in 6/17 patients in

660 fibrous tissue and bone, in 4/17 in bone marrow, in 3/17 in muscle, and in 2/17 in PA site skin. **D.** Number

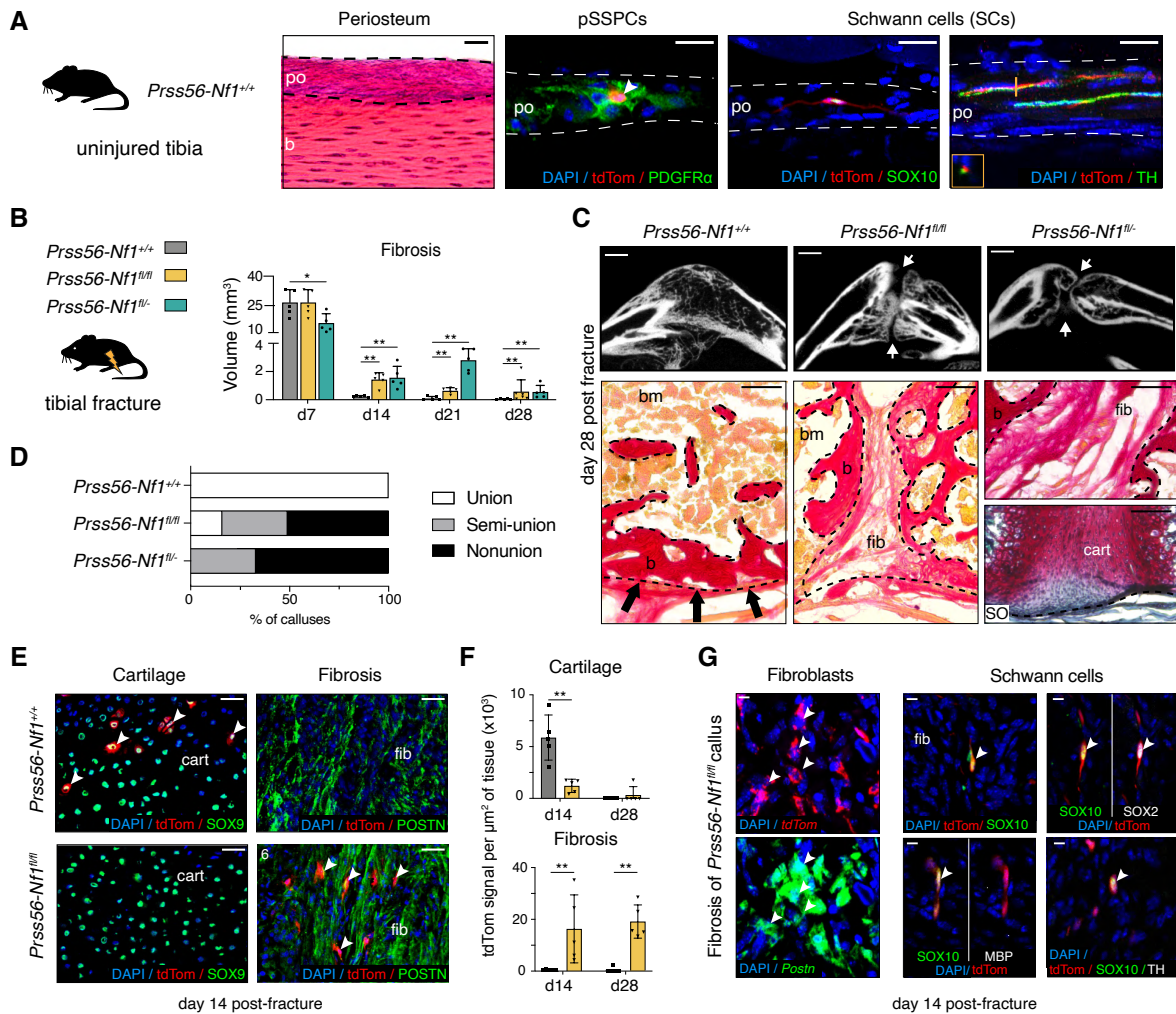
661 of patients with *NF1*-related CPT and isolated CPT carrying *NF1* biallelic inactivation. **E.** *NF1* genotyping

662 of periosteum and SSPCs from PA site shows the presence of *NF1* biallelic inactivation in 9/13 patients.

663 **F.** Left: experimental design. Cell populations were digested and sorted from PA periosteum of patient

664 P15 and the frequency of the 2 *NF1* point mutations (c.574C>T and c.5839C>T) was determined using
665 droplet digital PCR (ddPCR). Right: Percentage of the 2 mutations in the different cell populations
666 showing that Schwann cells and SSPCs carry both *NF1* hits, but not endothelial and immune cells. (n=
667 3 replicates). **G.** Phospho-ERK (pERK) immunofluorescence on periosteum sections showing number
668 of pERK+ cells in the periosteum from PA site compared to the periosteum from IC (white arrows).
669 Quantification of the percentage of pERK+ cells in the periosteum from PA and IC (n=5-6 patients per
670 group). **H.** Co-immunofluorescence of pERK and CD90, SOX10, CD31, CD68 and α SMA on PA
671 periosteum sections. **I.** Quantification of pERK+ cells in PA periosteum compared to IC periosteum (n=
672 5-6 patients per group). ** $p < 0.01$. BM: Bone marrow. Endo: endothelial cells. Scale bars: 50 μ m.
673

Figure 2



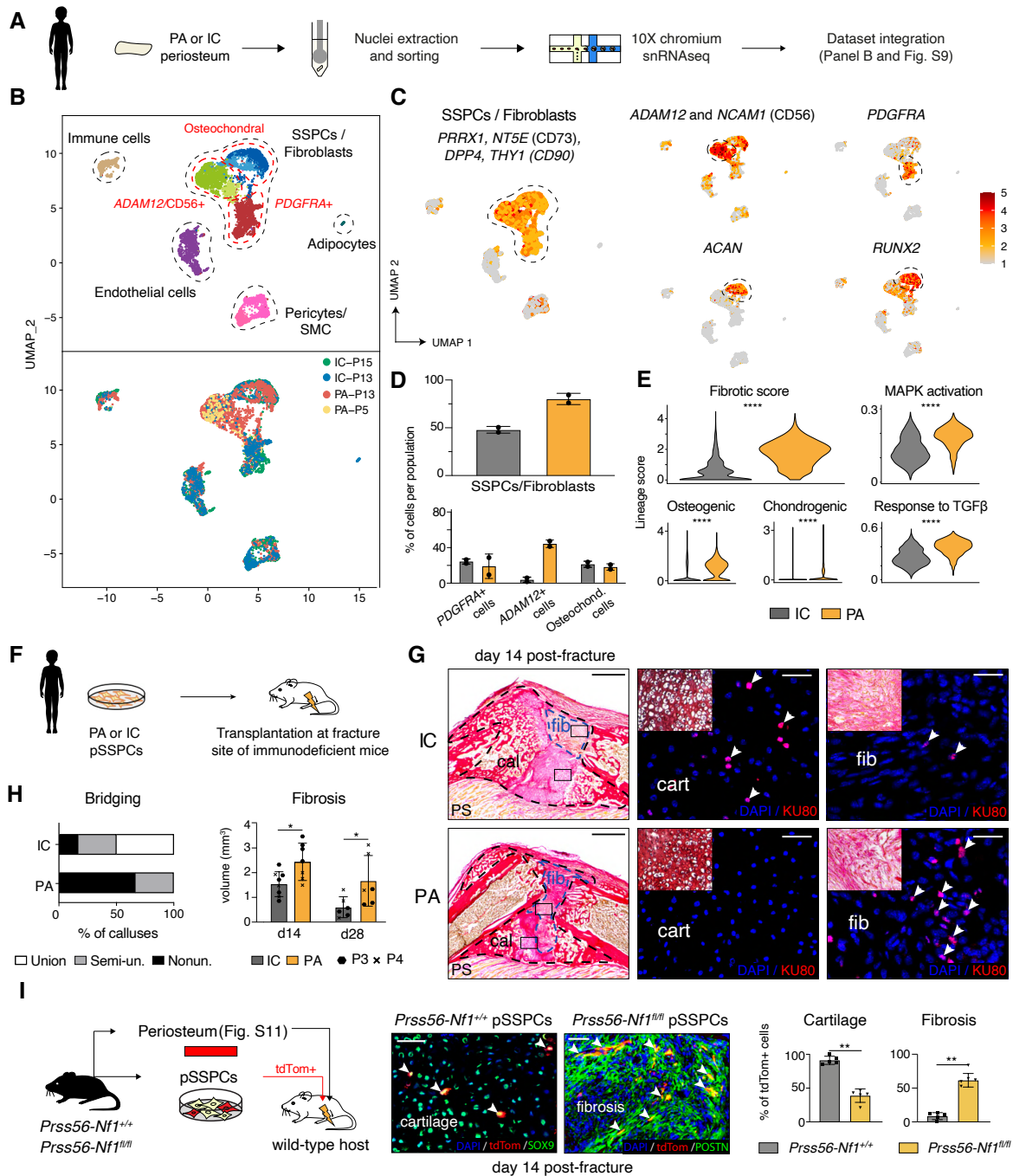
674

675 **Figure 2: Tibial pseudarthrosis in mice lacking *Nf1* gene in boundary cap-derived pSSPCs and**
 676 **Schwann cells**

677 **A.** Longitudinal sections of uninjured tibia periosteum (po) from 3-month-old *Prss56-Nf1^{+/+}* mice stained
 678 with Hematoxylin-Eosin and immunofluorescence on adjacent sections showing tdTom+ periosteal
 679 skeletal stem/progenitor cells (pSSPCs) expressing PDGFR α and tdTom+ Schwann cells (SCs)
 680 expressing SOX10 along TH+ nerves (orange box: transverse imaging). **B.** Left: Experimental design of
 681 tibial fracture in *Prss56^{Cre}; R26^{tdTom}; Nf1^{+/+}* (*Prss56-Nf1^{+/+}*) control, *Prss56^{Cre}; R26^{tdTom}; Nf1^{fl/fl}* (*Prss56-*
 682 *Nf1^{fl/fl}*) and *Prss56^{Cre}; R26^{tdTom}; Nf1^{fl/-}* (*Prss56-Nf1^{fl/-}*) mutant mice. Right: Histomorphometric
 683 quantification of the volume of callus fibrosis at days 7, 14, 21 and 28 post-fracture in *Prss56-Nf1^{+/+}*,
 684 *Prss56-Nf1^{fl/fl}* and *Prss56-Nf1^{fl/-}* mice (n=5-6 mice per group). **C.** Top: Representative microCT images
 685 of callus from *Prss56-Nf1^{+/+}*, *Prss56-Nf1^{fl/fl}* and *Prss56-Nf1^{fl/-}* mice at 28 days post-fracture, showing

686 absence of bone bridging in *Prss56-Nf1^{fl/fl}* and *Prss56-Nf1^{fl/-}* mutant mice (white arrows). Bottom, high
687 magnification of callus periphery showing bone bridging (black arrows) in *Prss56-Nf1^{+/+}* control mice,
688 and fibrosis and unresorbed cartilage (red, Safranin'O (SO)) in *Prss56-Nf1^{fl/fl}* and *Prss56-Nf1^{fl/-}* mutant
689 mice. **D.** Percentage of calluses from *Prss56-Nf1^{+/+}*, *Prss56-Nf1^{fl/fl}* and *Prss56-Nf1^{fl/-}* mice showing bone
690 union (white), semi-union (grey), or nonunion (black) on microCT scan at day 28 post-fracture (n=6 mice
691 per group). Bone union was significantly different between mutant and control mice (***, p=0.0067) but
692 not between the mutant groups (p=0.52). **E.** Lineage tracing of Prss56-expressing Boundary Cap (BC)-
693 derived tdTom+ cells (white arrowheads) in callus cartilage (labelled by SOX9) and fibrosis (labelled by
694 POSTN) of *Prss56-Nf1^{+/+}* and *Prss56-Nf1^{fl/fl}* mice 14 days after tibial fracture. **F.** Quantification of tdTom+
695 signal in cartilage and fibrosis of *Prss56-Nf1^{+/+}* and *Prss56-Nf1^{fl/fl}* mice 14- and 28-days post-fracture
696 (n=5 mice per group). **G.** RNAscope and immunofluorescence on callus sections of *Prss56-Nf1^{fl/fl}* mice
697 day 14 post-fracture show the presence of *Postn*-expressing tdTom+ fibroblasts and SOX10+tdTom+
698 SCs in fibrotic tissue. po: periosteum, b: bone, fib: fibrosis, cart: cartilage, bm: bone marrow, SO:
699 Safranin'O. p-value: * p < 0.05, ** p < 0.01. Scale bars: Panel A: 25µm. Panel C-microCT: 1mm. Panel
700 E/C-histology: 100µm. Panel G: 10µm.
701

Figure 3



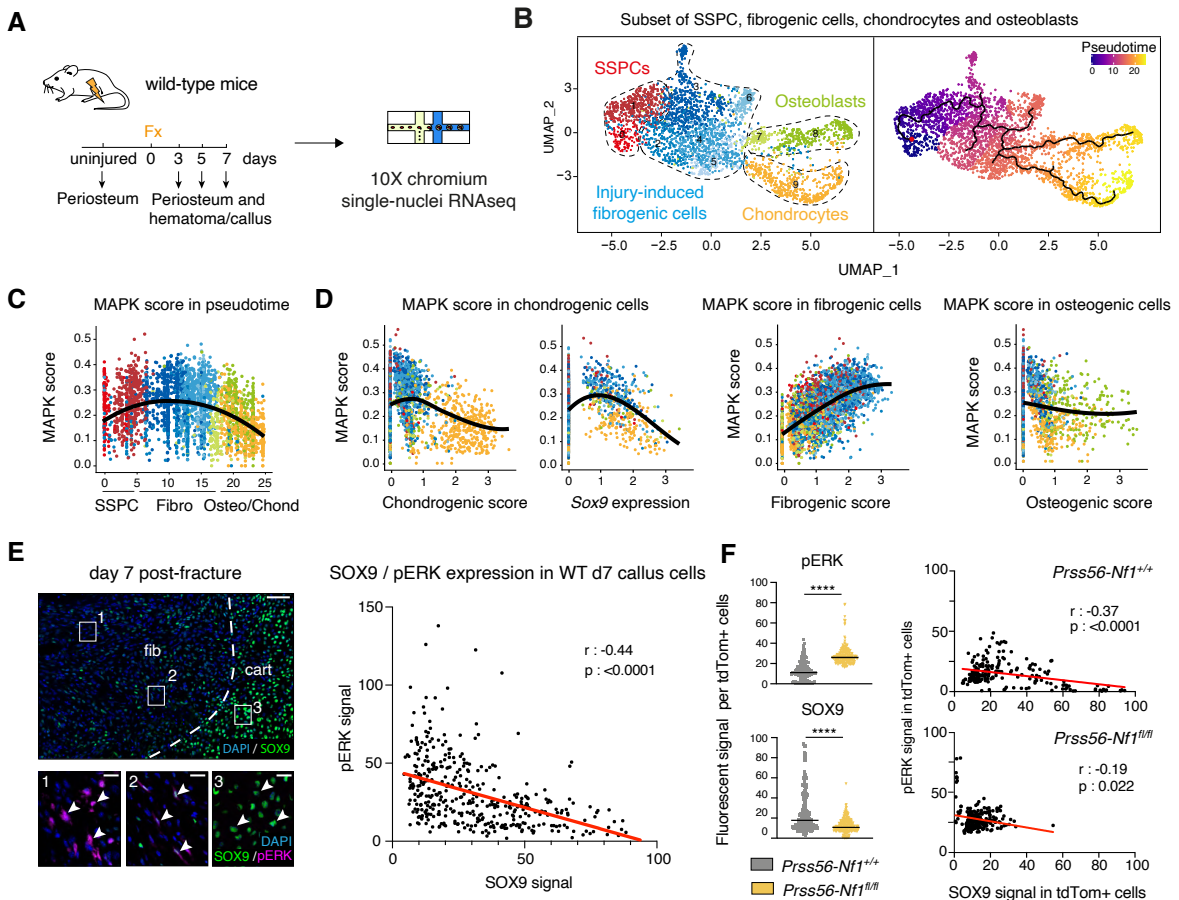
702

703 **Figure 3: Fibrotic fate of *NF1*-deficient periosteal SSPCs in patients with CPT and *Prss56-Nf1***
 704 ***KO* mice**

705 **A.** Experimental design. Nuclei were extracted from PA or IC periosteum, sorted, and processed for
 706 single-nuclei RNAseq. The datasets were integrated for analyses. **B.** UMAP projection of color-coded
 707 clustering (top) and sampling (bottom) of the integration of the datasets of IC periosteum from P15 (IC-

708 P15, green), IC periosteum from P13 (IC-P13, blue), PA periosteum from P13 (PA-P13, red) and PA
709 periosteum from P5 (PA-P5, yellow). **C.** Feature plots of the SSPC/fibroblast lineage score and
710 *ADAM12/NCAM1* (Neural Cell Adhesion Molecule 1), *PDGFRA*, *ACAN*, and *RUNX2* gene expression.
711 **D.** Percentage of cells from PA and IC samples in SSPC/fibroblast populations and in *ADAM12+*,
712 *PDGFRA+*, and osteochondral clusters. **E.** Violin plots of the fibrotic, osteogenic, chondrogenic, MAPK
713 activation, and cellular response to TGF β lineage score in IC and PA. **F.** Experimental design. PA or IC
714 pSSPCs from patients P3 and P4 were transplanted at the fracture site of immunodeficient mice. **G.**
715 Representative callus sections stained with Picrosirius (PS). High magnification of cartilage stained with
716 Safranin'O and fibrosis stained with PS and immunofluorescence of the human KU80 protein at day 14
717 post-fracture showing that IC pSSPC-derived cells are located mostly in cartilage while PA pSSPC-
718 derived cells are located in fibrosis (white arrow). **H.** Left: Percentage of callus grafted with PA or IC
719 pSSPCs showing union, semi-union, and nonunion at day 28 post-fracture. Right: Volume of fibrosis in
720 day 14 and 28 post-fracture callus of immunodeficient mice grafted with human pSSPCs from IC and
721 PA (n=6-8 mice per group). **I.** Left: Experimental design. Periosteum or cultured tdTom⁺ periosteal
722 skeletal stem/progenitor cells (pSSPCs) were isolated from *Prss56-Nf1^{+/+}* or *Prss56-Nf1^{fl/fl}* mice and
723 transplanted at the fracture site of wild-type hosts. Middle: Representative images of the contribution of
724 grafted tdTom⁺ cells (white arrows) showing cells from *Prss56-Nf1^{+/+}* mice detected in cartilage (labelled
725 by SOX9) and cells from *Prss56-Nf1^{fl/fl}* mice detected in fibrosis (labelled by POSTN). Right: Percentage
726 of grafted tdTom⁺ cells in cartilage and fibrosis (n=5 mice per group). SMC: smooth muscle cells, cal:
727 callus, fib: fibrosis, cart: cartilage. p-value: * p < 0.05, ** p < 0.01, **** p < 0.0001. Scale bars: Panel G:
728 Low magnification: 1mm. High magnification: 100 μ m. Panel I: 100 μ m.

Figure 4



729

730 **Figure 4: Overactivation of MAPK pathway causes fibrotic differentiation of *Nf1*-deficient**
 731 **pSSPCs**

732 **A.** Experimental design of single nuclei RNAseq (snRNAseq) experiment. Nuclei were isolated from
 733 uninjured periosteum, or periosteum and hematoma of wild type mice at days 3, 5, and 7 post- tibial
 734 fracture, sorted, and processed for snRNAseq. **B.** UMAP projection of clustering and monocle
 735 pseudotime trajectory of the subset of SSPCs, injury-induced fibrogenic cells, osteoblasts, and
 736 chondrocytes from integrated uninjured, day 3, day 5, and day 7 post-fracture samples. The four
 737 populations are delimited by black dashed lines. **C.** Scatter plot of MAPK score along pseudotime. **D.**
 738 Scatter plots of MAPK score along chondrogenic lineage score, *Sox9* expression, fibrogenic, and
 739 osteogenic lineage scores. **E.** Immunofluorescence of SOX9 and phospho-ERK (pERK) in day 7 post-
 740 fracture callus section of wild type (WT) mice. Quantification and correlation of SOX9 and pERK signal
 741 per cell (red line) (n = 397 cells from 8 callus sections of 4 mice). Scale bars: low magnification, 150µm;

742 high magnification, 25µm. **F.** Left: Quantification of SOX9 and pERK fluorescent signal per tdTom+ cells
743 in day 7 post-fracture callus of *Prss56-Nf1^{+/+}* and *Prss56-Nf1^{fl/fl}* mice. Right: Correlation analysis of pERK
744 and SOX9 signals in tdTom+ cells in *Prss56-Nf1^{+/+}* (top) and *Prss56-Nf1^{fl/fl}* (bottom) mice (n = 209 to
745 238 cells from 9 sections of 3 mice per group). cart: cartilage, fib: fibrosis. ****: p < 0.0001.

746

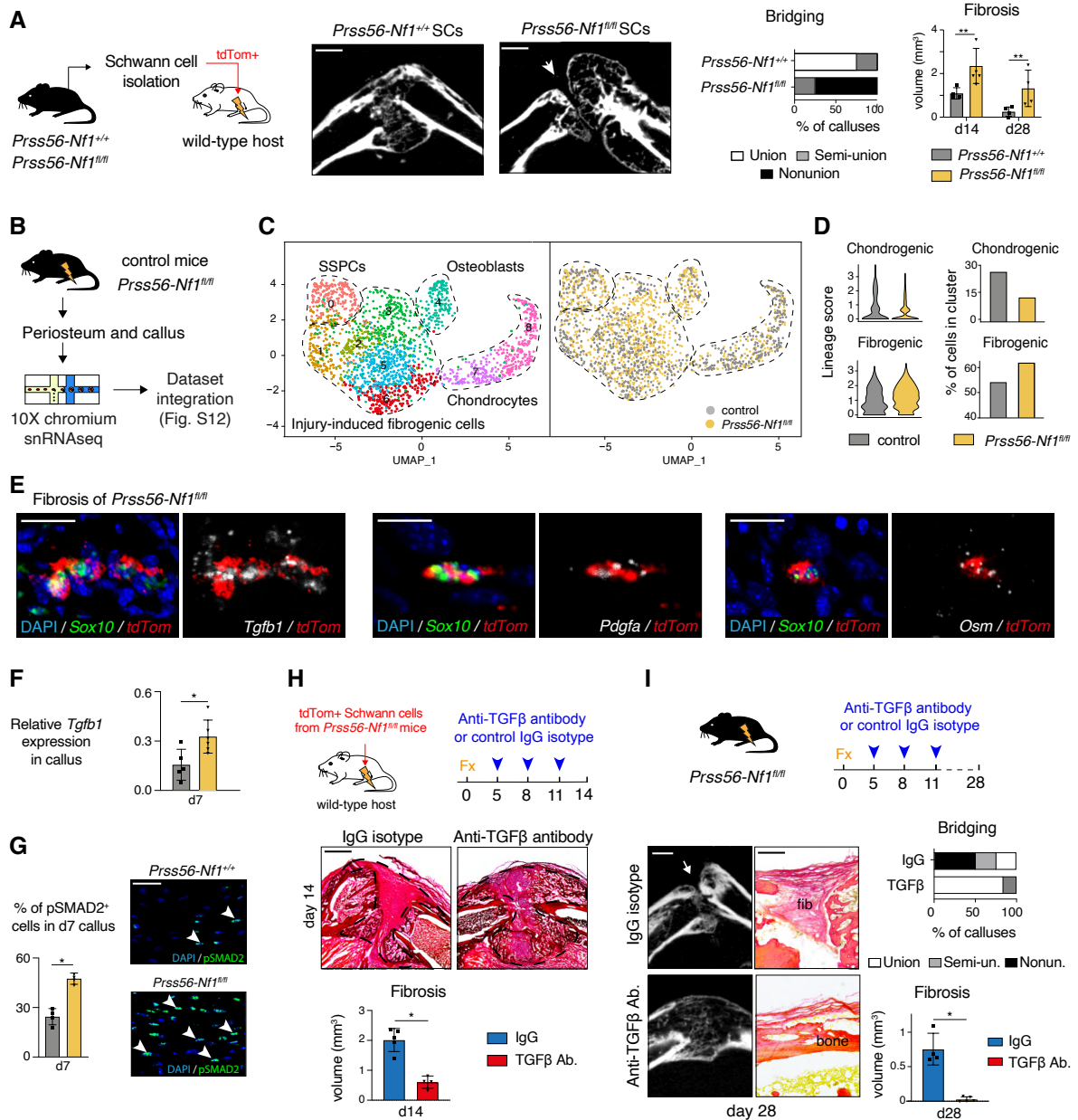
747

748

749

750

Figure 5



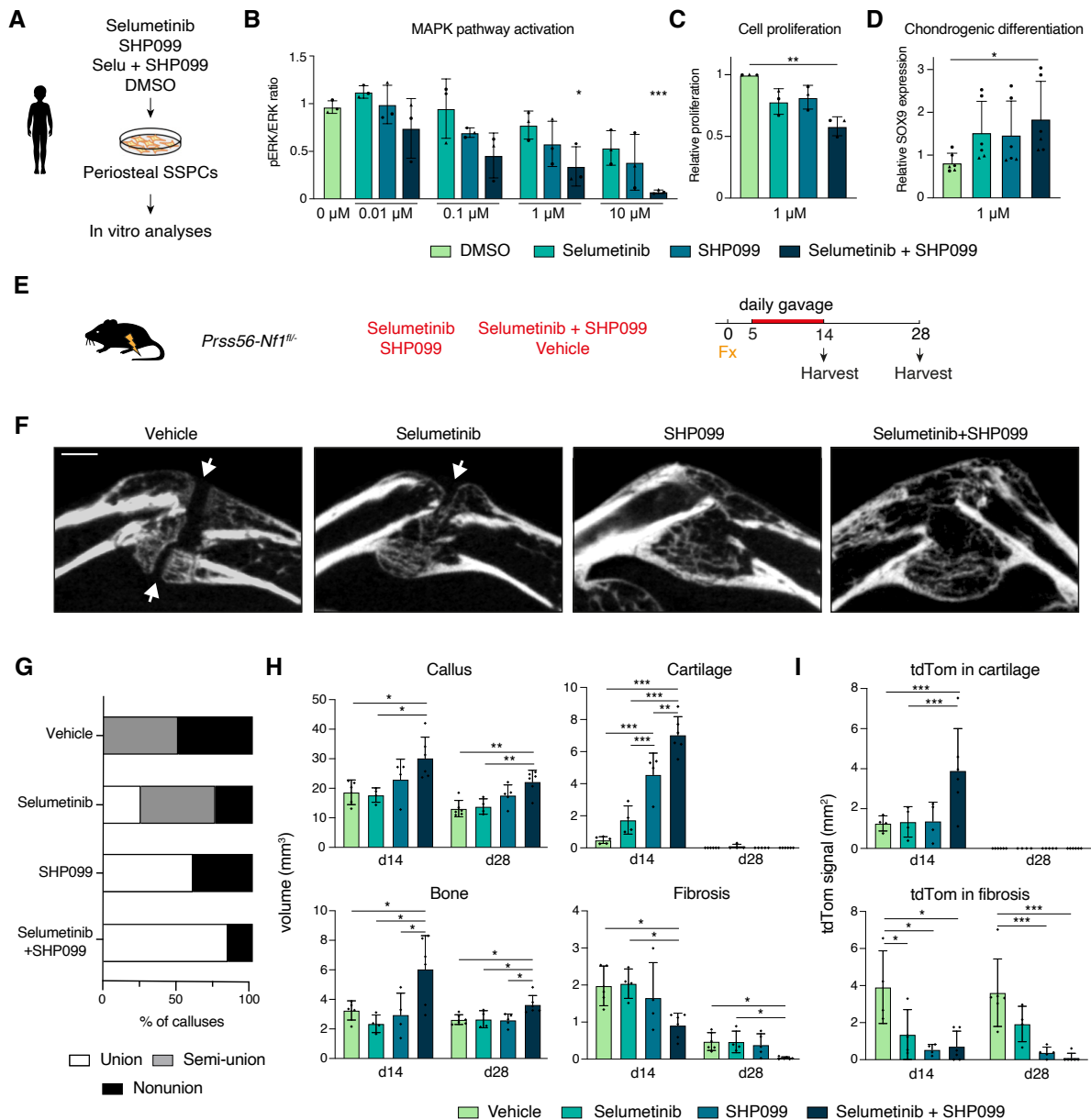
751

752 **Figure 5: Pro-fibrotic effect of *Nf1*-deficient Schwann cells in fibrous nonunion**

753 **A.** Left: Experimental design. tdTom+ Schwann cells (SCs) were isolated from *Prss56-Nf1^{+/+}* or *Prss56-*
 754 *Nf1^{fl/fl}* mice and transplanted at the fracture site of wild-type hosts. Middle: MicroCT images of 28 days
 755 post-fracture calluses of wild-type mice grafted with SCs from *Prss56-Nf1^{+/+}* or *Prss56-Nf1^{fl/fl}* mice,
 756 showing absence of bridging in mice grafted with *Nf1*-deficient SCs (white arrow). Right: Percentage of
 757 day 28 post-fracture calluses showing union, semi-union, or nonunion. Volume of callus fibrosis at 14
 758 and 28 days post-fracture (n=4-5 mice per group). **B.** Experimental design. Nuclei were isolated from
 759 periosteum and hematoma at day 7 post-fracture of control or *Prss56-Nf1^{fl/fl}* mice and processed for

760 snRNAseq. Datasets were integrated. **C.** UMAP projection of SSPC, injury-induced fibrogenic,
761 chondrogenic, and osteogenic cell subsets from the integrated day 7 post-fracture control and *Prss56-*
762 *Nf1^{fl/fl}* datasets. **D.** Violon plot of chondrogenic and fibrogenic lineage scores per dataset. Percentage of
763 cells per cluster. **E.** RNAscope experiment on day 7 post-fracture callus from *Prss56-Nf1^{fl/fl}* mice shows
764 the expression of *Tgfb1*, *Pdgfa*, and *Osm* by *Sox10*-, *tdTom*-expressing Schwann cells in callus fibrosis.
765 **F.** Relative expression of *Tgfb1* in day 7 post-fracture callus of *Prss56-Nf1^{+/+}* or *Prss56-Nf1^{fl/fl}* mice (n=5
766 mice per group). **G.** Percentage of phospho-SMAD2 positive (pSMAD2+) cells in the day 7 post-fracture
767 callus of *Prss56-Nf1^{+/+}* or *Prss56-Nf1^{fl/fl}* mice (n=4 mice per group). Representative pSMAD2
768 immunofluorescence of *Prss56-Nf1^{+/+}* or *Prss56-Nf1^{fl/fl}* callus. **H.** Top: Experimental design. Wild-type
769 mice grafted with tdTom+ Schwann cells from *Prss56-Nf1^{fl/fl}* mice were treated with blocking TGFβ
770 antibody or IgG1 control isotype at days 5, 8, and 11 post-fracture. Middle: Picrosirius staining of fracture
771 calluses at 14 days post-fracture. Bottom: Volume of callus fibrosis (n=4-5 mice per group). **I.** Top:
772 Experimental design. *Prss56-Nf1^{fl/fl}* mice were treated with blocking TGFβ antibody or IgG1 control
773 isotype at days 5, 8, and 11 post-fracture. Middle: MicroCT images of callus of *Prss56-Nf1^{fl/fl}* mice treated
774 with IgG1 isotype control or TGFβ blocking antibody at 28 days post-fracture. High magnification of the
775 callus periphery stained with Picrosirius. Bottom left: percentage of day 28 post-fracture calluses
776 showing union (white), semi-union (grey) or nonunion (black) on microCT scan. Bottom right: Volume of
777 callus fibrosis of *Prss56-Nf1^{fl/fl}* mice treated with blocking TGFβ antibody or IgG1 isotype control at 28
778 days post-fracture. (n=4-5 mice per group). p-value: * p < 0.05, ** p < 0.01. Scale bars: Panel A/H 1mm.
779 Panel E: 10μm. Panel G 50μm, panel I: Low magnification: 1mm, High magnification: 250 μm.

Figure 6



780

781 **Figure 6: Combined MEK and SHP2 inhibition prevents fibrous nonunion in *Prss56-Nf1* KO mice**

782 **A.** Experimental design. Periosteal SSCs from PA site of patients with CPT were treated with MEK

783 inhibitor (selumetinib), SHP2 inhibitor (SHP099), MEK and SHP2 inhibitors (selumetinib and SHP099),

784 or vehicle (DMSO) for in vitro analyses. **B.** MAPK pathway activation in pSSPCs from PA site treated

785 with selumetinib, SHP099, selumetinib and SHP099, or DMSO measured by the pERK/ERK ratio on

786 Western blot. Statistical significance was determined compared to DMSO control (n=3 patients). **C.**

787 Reduced in vitro proliferation of pSSPCs from PA site treated with combined selumetinib and SHP099

788 (n=3 patients). **D.** Increased in vitro chondrogenic differentiation measured by SOX9 expression of
789 pSSPCs from PA site treated with combined selumetinib and SHP099 (n=3 patients in duplicates). **E.**
790 Experimental design. *Prss56-Nf1^{fl/-}* mice were treated by oral gavage with selumetinib, SHP099,
791 selumetinib and SHP099, or vehicle from days 5 to 14 post-fracture. **F.** Representative microCT images
792 of callus from *Prss56-Nf1^{fl/-}* mice at 28 days post-fracture, with bone bridging indicated by white arrows.
793 **G.** Percentage of calluses from treated and control *Prss56-Nf1^{fl/-}* mice showing bone union (white), semi-
794 union (grey), or nonunion (black) on microCT scan at day 28 post-fracture (n=4-6 mice per group). **H.**
795 Volume of callus, cartilage, bone, and fibrosis at days 14 and 28 post-fracture in treated and control
796 *Prss56-Nf1^{fl/-}* mice (n=4-6 mice per group). **I.** Surface of tdTom signal in cartilage and fibrosis of day 14
797 and 28 callus from treated and control *Prss56-Nf1^{fl/-}* mice. Scale bars: 1mm. p-value: * p < 0.05, ** p <
798 0.01, *** p < 0.001.
799